

Article

Characterization of In-Situ TiB/TiC Particle-Reinforced Ti-5Al-5Mo-5V-3Cr Matrix Composites Synthesized by Solid-State Reaction with B₄C and Graphite through SPS

Steffen Grütznert^{1,*}, Lutz Krüger¹, Markus Radajewski¹ and Ines Schneider²

¹ Institute of Materials Engineering, TU Bergakademie Freiberg, Gustav-Zeuner-Str. 5, 09599 Freiberg, Germany; krueger@ww.tu-freiberg.de (L.K.); Markus.Radajewski@iwt.tu-freiberg.de (M.R.)

² Bundeswehr Research Institute for Materials, Fuels and Lubricants (WIWeB), Institutsweg 1, 85435 Erding, Germany; InesSchneider@bundeswehr.org

* Correspondence: Steffen.Gruetzner@iwt.tu-freiberg.de; Tel.: +49-3731-394-110

Received: 27 April 2018; Accepted: 22 May 2018; Published: 24 May 2018



Abstract: In-situ TiB/TiC particle-reinforced titanium matrix composites (TMCs) based on a near- β Ti-5Al-5Mo-5V-3Cr alloy (Ti-5553) were synthesized by solid-state reaction with B₄C and graphite particles during spark plasma sintering (SPS). In this study, investigations were focused on the influence of the molar TiB:TiC ratio on the mechanical properties of the composites. With respect to the adjustment of the molar TiB:TiC ratio, the formation of stoichiometric TiC or nonstoichiometric TiC_y was considered as the literature provides conflicting information in this respect. Furthermore, the solid-state reaction behavior influenced by the matrix alloying elements is discussed in comparison to a pure titanium matrix. The hardness, compressive strength and bending strength of the TMCs were improved successfully due to the TiB and TiC particles maintaining acceptable levels of ductility. However, X-ray diffraction experiments revealed that for the adjustment of the molar TiB:TiC ratio, the stoichiometry of the TiC_y particles formed must be considered as nonstoichiometric TiC_{0.5} resulted from the solid-state reaction of carbon and titanium. Compared to TMCs with pure titanium matrices, more sluggish solid-state reaction kinetics were observed. This was attributed to the matrix alloying elements molybdenum, vanadium and chromium, which formed solid solutions within the reinforcing particles.

Keywords: SPS—spark plasma sintering; Ti-5Al-5Mo-5V-3Cr; titanium matrix composites; microstructures; X-ray analysis; electron probe microanalysis; TiB:TiC ratio; mechanical properties

1. Introduction

In recent decades, materials research has increasingly focused on the development of titanium matrix composites (TMCs) due to their outstanding properties—combining high specific strength, specific stiffness, and hardness with heat- and/or corrosion resistance [1–4]. An effective method for improving the properties of titanium or titanium alloy-based composite materials is their reinforcement through the introduction of ceramic particles. Relating to this, in-situ particle reinforced metal matrix composites (MMCs) exhibiting excellent mechanical properties owing to the formation of stable ceramic reinforcements during processing are reported in the literature including a wide range of matrix materials like titanium, aluminum, copper, nickel or iron along with borides, carbides, oxides and nitrides [5]. Especially with respect to the TMCs, investigations have shown that the most significant strengthening effect is achieved by reinforcement with titanium carbide particles (TiC) and whisker-shaped titanium boride particles (TiB) [6–16]. The high reactivity between titanium, boron

and carbon at elevated temperatures enables the in-situ generation of the reinforcing particles through liquid-solid or solid-solid reactions during processing. As a consequence, in-situ particle-reinforced MMCs have been synthesized successfully by means of powder metallurgy through the addition of reactive powders, e.g., B₄C, TiB₂, CrB, Cr₃C₂, MoB, BN (or elemental boron and carbon) to a titanium matrix powder [7,17,18]. Reactions relevant for the in-situ formation of TiB and TiC are presented below:



However, the exothermic solid-state reactions between titanium and boron or titanium and carbon are diffusion-controlled processes [19–22]. In particular, the reaction between titanium and B₄C at temperatures between 1000 °C and 1300 °C results in the formation of a complex reaction layer sequence Ti-TiC_{0.5}-TiB-TiB₂-B₄C. This behavior is directly related to the higher diffusivity of carbon in β-titanium compared to that of boron in β-titanium and titanium self-diffusion. The growth kinetics of the reaction layer are characteristic of the diffusion-controlled process, which follows a parabolic law [20]. Furthermore, and in contrast to the intermetallic compound TiB with its strong stoichiometric composition, the formation of stoichiometric TiC is debatable due to its disposition with respect to vacancy formation within the carbon sub-lattice. The composition of non-stoichiometric TiC_y extends from TiC_{0.47} to TiC_{0.97} [23,24]. However, with respect to reactions (2) and (3), very little information is available in the literature regarding the actual stoichiometry of the TiC particle reinforcement within the TMCs. Considering the equilibrium Ti-C phase diagram within the typical temperature range applied for the solid-state reactions, where β-Ti and TiC_y or TiC_y and carbon (graphite) exist next to each other (~920 °C < T < ~1646 °C), the titanium carbide compositions at the β-Ti/TiC_y and TiC_y/C interfaces are listed in Table 1 [25,26]:

Table 1. Selected stoichiometric compositions of TiC_y according to [25,26].

| Temperature in °C | C/Ti Ratio <i>y</i> in TiC _{<i>y</i>} | |
|-------------------|--|--------------------------------------|
| | Interface β-Ti/TiC _{<i>y</i>} | Interface TiC _{<i>y</i>} /C |
| 920 | 0.56 | 0.97 |
| 1200 | 0.53 | 0.97 |
| 1646 | 0.47 | 0.97 |

Assuming the formation of non-stoichiometric TiC_y and considering the limiting cases of the TiC_y stoichiometry mentioned above (with ~0.5 ≤ *y* ≤ ~1), reactions (2) and (3) can be adjusted, as shown below:



Hence, the molar fractions of TiC_y formed by these reactions increase up to a double value with decreasing stoichiometry. A similar behavior is observed during the synthesis of in-situ TiC particle reinforced 316 L stainless steel matrix composites using the selective laser melting technique (SLM), where sub-stoichiometric TiC_y is formed due to the reaction of titanium and carbon powders [27]. Despite these well-known relationships with respect to the solid-state reaction behavior between titanium and carbon, however, most reported studies dealing with TiC particle-reinforced TMCs assume the formation of stoichiometric TiC according to reactions (2) and (3), and further not considering the influences of the real TiC particle stoichiometry. For instance, Lu et al. [28] and Wang et al. [29] investigate the influence of the TiB:TiC ratio adjustment on the mechanical properties

of particle-reinforced TMCs that were processed by liquid-solid reactions between titanium alloys and B_4C and/or graphite, which served as reactive powders. For the adjustment of the TiB and TiC phase contents, they combined reactions (2) and (3) while assuming the formation of stoichiometric TiC and using graphite as an additional source of carbon to B_4C . It was found that TMCs with a calculated adjusted molar ratio of TiB:TiC = 1:1 exhibited a higher tensile strength than the phase composition with minor TiC content. In addition, an improved Young's modulus and slightly increased ductility were measured by Lu. Unfortunately, no information is given in these studies about the TiC stoichiometry generated within the TMCs investigated. Thus, an underestimation of the real TiC phase content seems possible.

The present study analyzes the influence of the molar TiB:TiC ratio on the mechanical properties of particle-reinforced TMCs based on a near- β Ti-5Al-5Mo-5V-3Cr matrix. In particular, the current investigations focused on improvements in hardness, stiffness, compressive strength and bending strength. TMCs were processed by the solid-state reaction of distinct powder mixtures during spark plasma sintering (SPS). Furthermore, the in-situ TiC_y particle stoichiometric compositions and phase contents were determined. Finally, differences between calculated and real TiC phase contents within the TMCs are discussed under the aspect of the desired adjustment of the molar TiB:TiC ratio.

2. Materials and Methods

Exhibiting a similar particle-size distribution, Ti-5Al-5Mo-5V-3Cr powder and commercially pure Ti powder (Ti-5553 and CP-Ti Grade 1, TLS Technik GmbH & Co Spezialpulver KG, Bitterfeld-Wolfen, Germany) were used as raw materials in this study, along with B_4C powder (abcr GmbH, Karlsruhe, Germany) and graphite powder (purity: 99.9995%, abcr GmbH). Data on the initial powder's chemical compositions and particle-size distributions are given in Tables 2 and 3. The values d_{10} , d_{50} and d_{90} represent the maximum particle diameters for 10%, 50% and 90% of the particles in each powder.

Table 2. Initial powders—chemical composition.

| Ti-5553 | | | | | | | | |
|-------------------|---------|----------|---------|---------|---------|---------|----------|---------|
| Composition wt.-% | Ti bal. | Al 5.22 | Mo 5.08 | V 4.97 | Cr 2.86 | Fe 0.30 | O 0.14 | N 0.013 |
| CP-Ti | | | | | | | | |
| Composition wt.-% | Ti bal. | Fe 0.069 | N 0.008 | O 0.068 | C 0.007 | - | | |
| B_4C | | | | | | | | |
| Composition wt.-% | B bal. | C 21.90 | N 0.20 | O 1.40 | Si 0.11 | Al 0.01 | Fe <0.01 | - |

Table 3. Initial powders—particle-size distributions measured by laser diffraction particle-size analysis.

| Values in μm | d_{10} | d_{50} | d_{90} |
|-----------------------|----------|----------|----------|
| Ti-5553 | 11.12 | 26.56 | 42.64 |
| CP-Ti | 11.83 | 24.97 | 41.27 |
| B_4C | 0.51 | 1.08 | 1.96 |
| Graphite ¹ | 7.73 | 32.31 | 82.99 |

¹ particles were dispersed in silicone oil prior to particle size measurement.

The powder mixtures were prepared on the basis of reaction Equations (2) and (3) with regard to the adjustment of the molar TiB:TiC ratio, as well as for the TiC_y stoichiometry. Assuming complete conversion of the reactive powders during the solid-state reaction with titanium, the powder mixtures were calculated such that they would result in the formation of a 12 vol.-% total particle reinforcement

content within the TMCs. In this regard, the appropriate compositions of the powder mixtures and corresponding designations of the final TMCs are listed in Table 4.

Table 4. Calculated compositions of the powder mixtures and theoretical molar TiB:TiC_y ratios for the corresponding TMCs.

| Theoretical Reaction Equation | Theoretical Total Ceramic Content | Reactive Powder Addition | Theoretical Molar TiB:TiC _y Ratio | TMC Designation |
|--|-----------------------------------|---|--|----------------------------------|
| $(x + 5)\text{Ti} + \text{B}_4\text{C} \rightarrow x\text{Ti} + 4\text{TiB} + \text{TiC}_{1.0}$ | 12 vol.-% | 4.0 vol.-% B ₄ C | TiB:TiC _{1.0} = 4:1 | TMC-A (Ti-5553) TMC-A (CP-Ti) |
| $(x + 8)\text{Ti} + \text{B}_4\text{C} + 3\text{C} \rightarrow x\text{Ti} + 4\text{TiB} + 4\text{TiC}_{1.0}$ | 12 vol.-% | 2.5 vol.-% B ₄ C 1.8 vol.-% C | TiB:TiC _{1.0} = 1:1 | TMC-B (Ti-5553) TMC-B (CP-Ti) |
| $(x + 8)\text{Ti} + \text{B}_4\text{C} + \text{C} \rightarrow x\text{Ti} + 4\text{TiB} + 4\text{TiC}_{0.5}$ | 12 vol.-% | 2.6 vol.-% B ₄ C 0.6 vol.-% C | TiB:TiC _{0.5} = 1:1 | TMC-C (Ti-5553) TMC-C (CP-Ti) |

The initial powders were mixed in a planetary ball mill (Pulverisette 6, Fritsch GmbH, Idar-Oberstein, Germany) for four hours at a rotational speed of 110 rpm in a container made of hardened steel and using hardened Cr-steel balls with a diameter of 10 mm. A powder-to-ball mass ratio of 1:5 was selected during the mixing operation. Cylindrical samples with a diameter of 40 mm and final heights of 4 to 8 mm were consolidated in a vacuum by spark plasma sintering (SPS) using an FCT-HP D 25/2-2 apparatus (FCT Systeme GmbH, Effelder-Rauenstein, Germany). The powder mixtures were heated at a rate of 100 K/min while increasing the pressure from 4 MPa at 450 °C to 51 MPa at 1200 °C. This was followed by a dwell time of 15 min while the pressure was kept constant. Finally, the pressure was reduced to 4 MPa within 10 s prior to uncontrolled cooling. The microstructures and phase compositions of the TMCs based on Ti-5553 were compared to TMCs with a CP-Ti matrix processed in an analogous manner. Furthermore, the effect of the particle reinforcement on the mechanical properties was evaluated with respect to samples consisting of pure Ti-5553. Prior to the microstructural investigations using light microscopy (Neophot 30 optical microscope, Carl Zeiss Jena GmbH, Jena, Germany) and SEM (MIRA3 XMU, TESCAN, Brno, Czech Republic), the samples had to be prepared by mechanical grinding and polishing, followed by chemical-mechanical polishing and a final etching process with Kroll's reagent. The chemical composition of distinct microstructural components within the TMCs was measured by electron probe microanalysis EPMA (JXA 8900 RL, JEOL, Tokyo, Japan). A detailed description of the phase analysis and the determination of lattice parameters derived from X-ray diffraction XRD patterns is described below and was carried out similarly to the experiments presented by Grütznert et al. [30]. The XRD experiments were performed in Bragg-Brentano geometry using a SEIFERT-FPM URD6 diffractometer (Seifert-Freiberger Präzisionsmechanik, Freiberg, Germany) equipped with a sealed X-ray tube, applying a Cu anode, and operating parameters of 40 kV/30 mA. The data evaluation process employed Rietveld-like whole powder pattern fitting [31] using the Maud software package (Version 2.4.6, University of Trento, Trento, Italy) [32]. Phase identification was based on the following PDF database entries: bcc-Ti (#44-1288: space group Im-3m), hcp-Ti (#44-1294: space group P6₃/mmc), TiB (#04-05-6142: space group Pnma), TiB₂ (#35-0741: space group P6/mmm), Ti₃B₄ (#19-1368: space group Immm), TiC_{1.0} (#32-1383: space group Fm-3m), B₄C (#35-0798: space group R-3m) and graphite (#56-0159: space group P6₃/mmc). The refinement was implemented with the lattice parameters, isotropic crystallite size and microstrain as well as the relative volume fractions of the phases representing the refinable parameters.

The hardness was measured using Vickers indentations (EMCOTEST M4U-025, EMCO-TEST Prüfmaschinen GmbH, Kuchl, Austria) introduced at an indentation load of 49.03 N. Samples for both the compression tests and the bending tests were cut from the sintered bodies by electrical discharge machining. The compression tests were carried out on cylindrical samples with equal diameters and heights of 6 mm at a strain rate of 10⁻³ s⁻¹ at room temperature using an MTS 810 servo-hydraulic

testing machine (MTS, Eden Prairie, MN, USA). In the 3-point bending tests bar-shaped samples (dimensions 25 mm × 2.5 mm × 2.0 mm) with ground surfaces were loaded up to points immediately below failure and up to their failure on a universal testing machine (inspekt 10 desk, Hegewald & Peschke, Nossen, Germany). Meanwhile, the load-deflection curves were recorded. The deflection was measured close to the sample by a laser interferometer (OFV-525, Polytec, Waldbronn, Germany) at the upper punch of the bending test setup. Finally, the increase in stiffness through the particle reinforcements was described in terms of the bending modulus E_b , which was calculated from the measured load-deflection curves.

3. Results and Discussion

3.1. Structural Characterization

Figure 1 shows SEM micrographs of the initial powders used in the study. The powder particles of Ti-5553 and CP-Ti were almost spherical, as can be seen in Figure 1a,b. In contrast, the considerably smaller B_4C particles presented in Figure 1c exhibited an angular shape, while the graphite powder consisted of large particles with a high aspect ratio between length and thickness, and fine, flake-shaped particles which were partly arranged in clusters, Figure 1d.

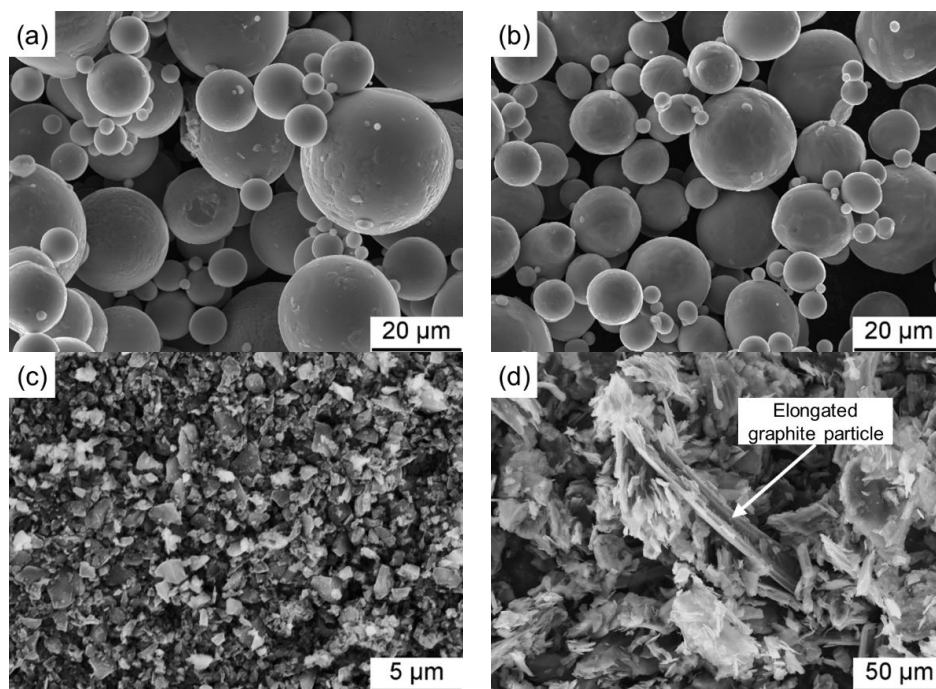


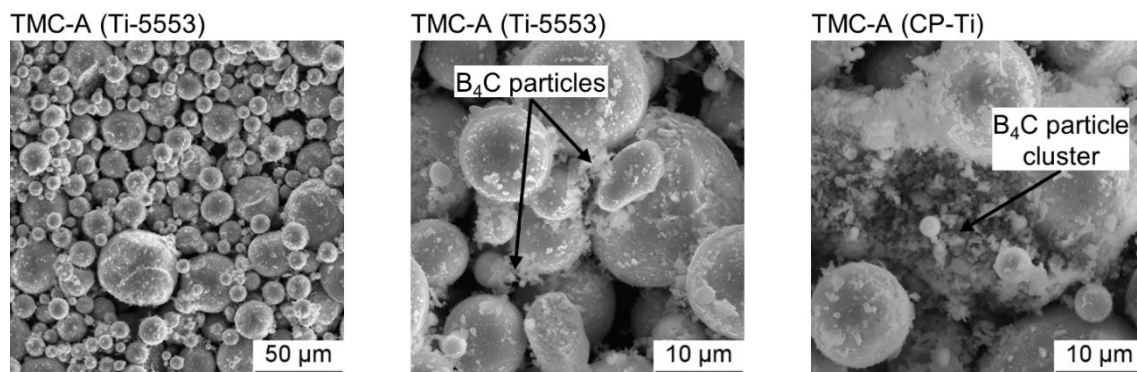
Figure 1. Scanning electron micrographs (secondary electron contrast SEM-SE) of the initial powders: (a) Ti-5553; (b) CP-Ti; (c) B_4C and (d) graphite.

The presence of these elongated graphite particles—which exhibited lengths of more than double the diameter of to the largest titanium particles—was not expected, as the powder was previously classified by a sieve with a mesh size of approximately 44 μm (325 mesh). It was believed that the large d_{90} value of 82.99 μm for graphite given in Table 3 was the result of significant particle agglomeration following the powder sieving process. However, these elongated particles were apparently able to pass through the sieve due to their considerably lower diameters.

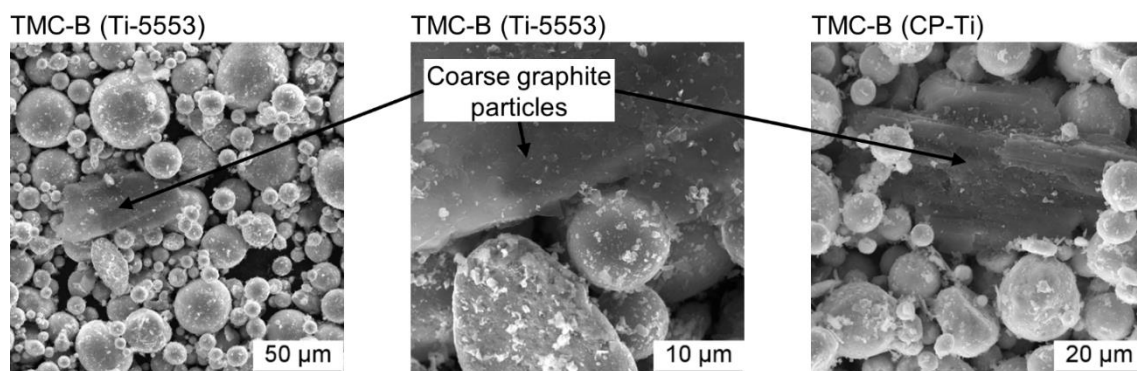
Survey and detailed SEM micrographs of the powder mixtures are shown in Figure 2. As can be seen for the mixtures consisting of Ti-5553 or CP-Ti and B_4C in Figure 2a, the B_4C particles were distributed around and adhered to the surfaces of the undeformed matrix particles. Additionally, a few local clusters were observed that consisted of agglomerated B_4C particles. The powder mixtures

consisting of the matrix particles B_4C and graphite in Figure 2b,c did not significantly differ in appearance except in terms of the scattered presence of coarse graphite particles. Unfortunately, with respect to the SEM micrographs at higher magnifications in Figure 2b,c a morphological distinction could not be made between the B_4C and the smaller graphite particles attached to the matrix particle surfaces.

(a) Powder mixtures of TMC-A



(b) Powder mixtures of TMC-B



(c) Powder mixtures of TMC-C

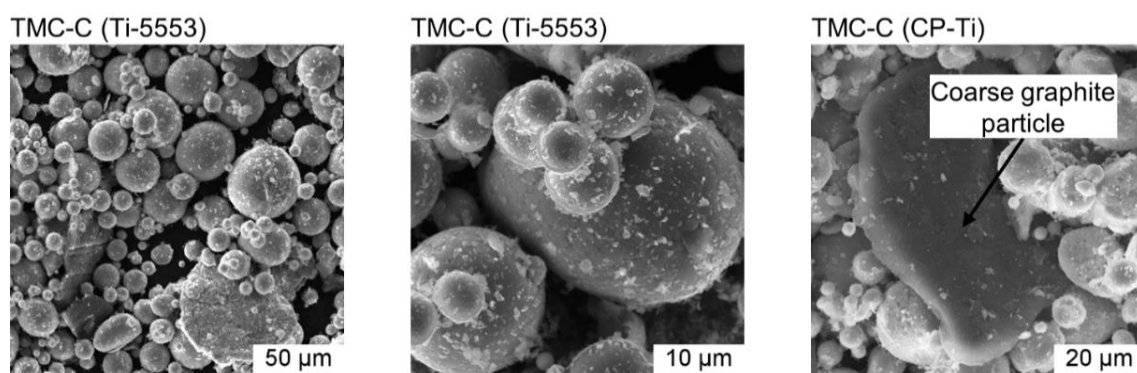


Figure 2. SEM-SE micrographs of the powder mixtures at lower and higher magnifications: (a) TMC-A; (b) TMC-B and (c) TMC-C.

The microstructures of the consolidated TMCs are shown by the micrographs of the etched surfaces in Figure 3. Within the light optical micrographs in Figure 3a–f the matrix particles and reinforcing particles can be distinguished—with the former appearing white to light grey and the latter appearing a darker grey. With respect to the reinforcements, TiB and TiC particles exhibited different

morphologies. The TiB formed whiskers while the TiC particles were almost plate-shaped. Regarding the TMCs based on Ti-5553—visible in Figure 3a,c,e—the reinforcing particles were predominantly arranged around the initial matrix particle surfaces. However, markedly fewer reinforcing particles were located within the matrix particles. In contrast, the reinforcing particles were distributed more homogeneously within the matrix of the TMCs based on CP-Ti—see Figure 3b,d,f.

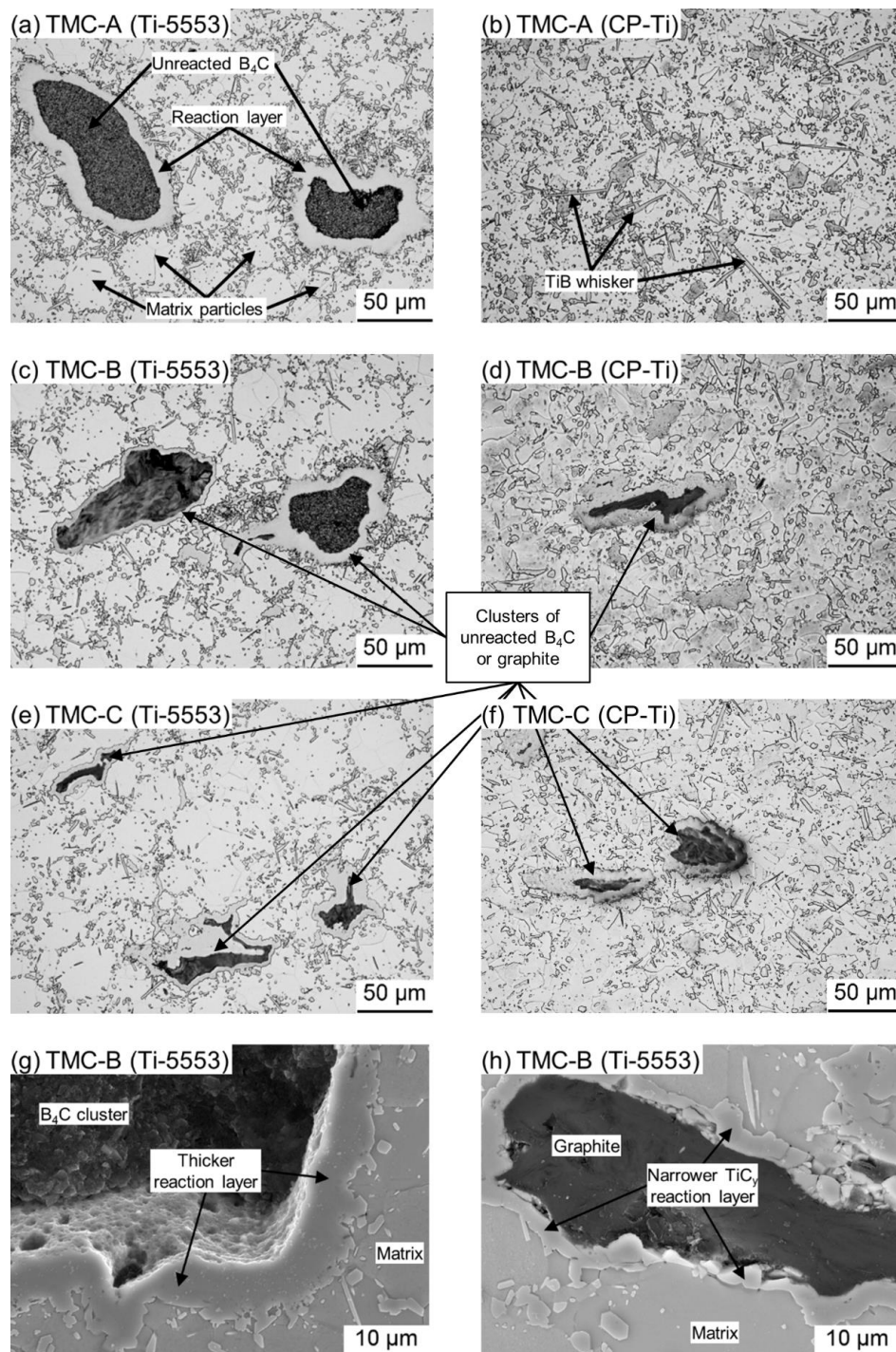


Figure 3. Micrographs of the consolidated titanium matrix composites (TMCs) etched with Kroll's reagent; (a–f) light optical micrographs; (g,h) SEM-SE.

Except for TMC-A (CP-Ti), large clusters consisting of unreacted B_4C and/or graphite particles appearing black-to-dark grey were present in the microstructures of the TMCs. The number of these clusters was lower for TMC-C consisting of the initial powder mixtures with the lowest contents of B_4C and graphite. All of these clusters were surrounded by a reaction layer at their interfaces to the adjacent matrix particles. More microstructural details are shown at higher magnifications by the SEM-SE micrographs in Figure 3g,h for the TMC-B (Ti-5553) sample.

The cluster in Figure 3g consisted of many small angular particles with particle diameters of less than $2\ \mu\text{m}$. Some of these particles were lost during the preparation, as can be seen by the sharp edge at the interface to the reaction layer. The measured thickness of the reaction layer was about $4\text{--}10\ \mu\text{m}$, which was in agreement with the reaction kinetics study concerning the Ti- B_4C system described by Mogilevsky et al. [20]. Furthermore, the particle break-out mentioned was assumed to have resulted from the low degree of B_4C particle consolidation and, hence, from the low strength of the clusters, as the literature data postulates higher sintering temperatures of $1500\text{--}2050\ \text{°C}$ for effective densification of this material during SPS [33].

The cluster in Figure 3h shows a completely different microstructure, and it apparently consisted of only a few individual particles. The thickness of the reaction layer at the interface to the adjacent matrix particles was significantly lower, exhibiting values of less than $\sim 3\ \mu\text{m}$. These clusters were found independently of the matrix material, but only within the composites TMC-B and TMC-C, which contained graphite as a reactive powder. A couple of such clusters were analyzed by EPMA using a polished sample, where only carbon (approximately 100 vol.-%) was measured—confirming the presence of incompletely reacted graphite. The solid-state reaction between graphite and titanium (-alloy) is a complex diffusion-controlled process. As part of this process, a TiC_y reaction layer is formed at the interfaces between the graphite and the titanium, as described by Vansant and Phelps [34]. According to their study, the rate of TiC formation between graphite and titanium is controlled by the diffusion of titanium and carbon atoms through the carbide layer itself, and follows a parabolic correlation with time. At the same time, the inter-diffusion coefficient decreases with increasing TiC stoichiometry [35]. However, the stoichiometry within the TiC_y layer formed is not constant (see Table 1), but decreases from the graphite/TiC interface to the TiC/Ti interface [23]. The diffusivities of both C and Ti in titanium carbide are coupled, while the rate of mass transport and, hence, the growth rate of the TiC layer thickness is determined by the lower mobility of the titanium [36]. With respect to the sintering conditions applied ($T = 1200\ \text{°C}$ and $t = 15\ \text{min}$), the measured thickness of the TiC reaction layer is consistent with the data presented by Vansant and Phelps [34], i.e., calculated according to Wagner's treatment ($\sim 1\ \mu\text{m}$) or the Steady State treatment ($\sim 2\ \mu\text{m}$). Hence, the particle diameters of the graphite powder used in this study were too large to completely undergo chemical reaction with the matrix.

The different local distributions of the TiB and TiC particles within either the CP-Ti or the Ti-5553 matrices were not expected. Even the SEM micrographs of the initial powder mixtures were similar with respect to the arrangement of matrix, B_4C and/or graphite particles. One possible reason for the concentration of TiB and TiC particles at the initial Ti-5553 particle surfaces could have been the reduced diffusivities of Ti, B or C due to the alloying elements Al, Mo, V and Cr, which were dissolved within the Ti-5553 matrix particles. Hence, diffusion experiments were carried out to provide a better understanding of the differences in reaction kinetics between CP-Ti or Ti-5553 and B_4C . To this end, stacked powder layers consisting of B_4C /CP-Ti and B_4C /Ti-5553 were consolidated through SPS under sintering conditions identical to those used for the TMC samples. Subsequently, the elemental distributions in the region of the solid-state reactions were characterized by EPMA. It should be noted that it was not possible to perform EPMA line scans that crossed the entire reaction layer sequence, as the remaining B_4C did not densify at $1200\ \text{°C}$ and was completely lost during the sample preparation process. Nevertheless, a transition from the pure metal/alloy to TiB_2 was observed for both samples—see regions (I) and (II) in Figure 4. However, the thickness of region (I), i.e., the transition between CP-Ti or Ti-5553 and TiB_2 , was increased from $\sim 3\ \mu\text{m}$ (B_4C /CP-Ti

sample) to $\sim 6\mu\text{m}$ ($\text{B}_4\text{C}/\text{Ti-5553}$ sample). A similar behavior was observed for the TiB_2 layer thickness in region (II), where the measured values were again doubled from $\sim 2\mu\text{m}$ ($\text{B}_4\text{C}/\text{CP-Ti}$ sample) to $\sim 4\mu\text{m}$ ($\text{B}_4\text{C}/\text{Ti-5553}$ sample). In addition, Figure 5 shows that the alloying elements Mo, V and Cr formed solid solutions within the TiB_2 region, and may have caused the increase in the TiB_2 layer thickness. Several studies indicate that small to medium amounts of Mo, V and Cr can be dissolved in TiB and TiB_2 [37–39]. Unfortunately, there is a dearth of literature that would deal with the diffusion behavior within such solid solutions. However, considering the low diffusivity of boron (originating from the B_4C particles) in TiB_2 ($D_{1473\text{K}} \approx 1.2 \times 10^{-19} \text{m}^2\text{s}^{-1}$ [40]) in combination with the extended TiB_2 layer thickness, it can be assumed that the reaction kinetics between B_4C and Ti-5553 is more sluggish compared to CP-Ti. It may also have been possible that the mobility of the titanium diffusing from the matrix in the direction of the B_4C decreased due to the partial substitution of regular Ti atoms by Mo, V and Cr within the borides. The absence of TiC_y in the reaction area is associated with the significantly higher diffusivity of carbon compared to boron. According to the literature, in the early stage of B_4C conversion, in particular, carbon diffuses rapidly into the titanium matrix, leaving behind an area with high boron activity. In this area, the aforementioned $\text{B}_4\text{C-TiB}_2\text{-TiB}$ reaction layer sequence is then formed with respect to the decreasing boron content [19]. Further carbon diffusion within this reaction layer from the B_4C in the direction of the unreacted titanium proceeds at a significantly lower rate of diffusion. However, the $\text{TiC}_{0.5}$ particles nucleated in front of the reaction layer and, thus, were not detected by the EPMA measurement.

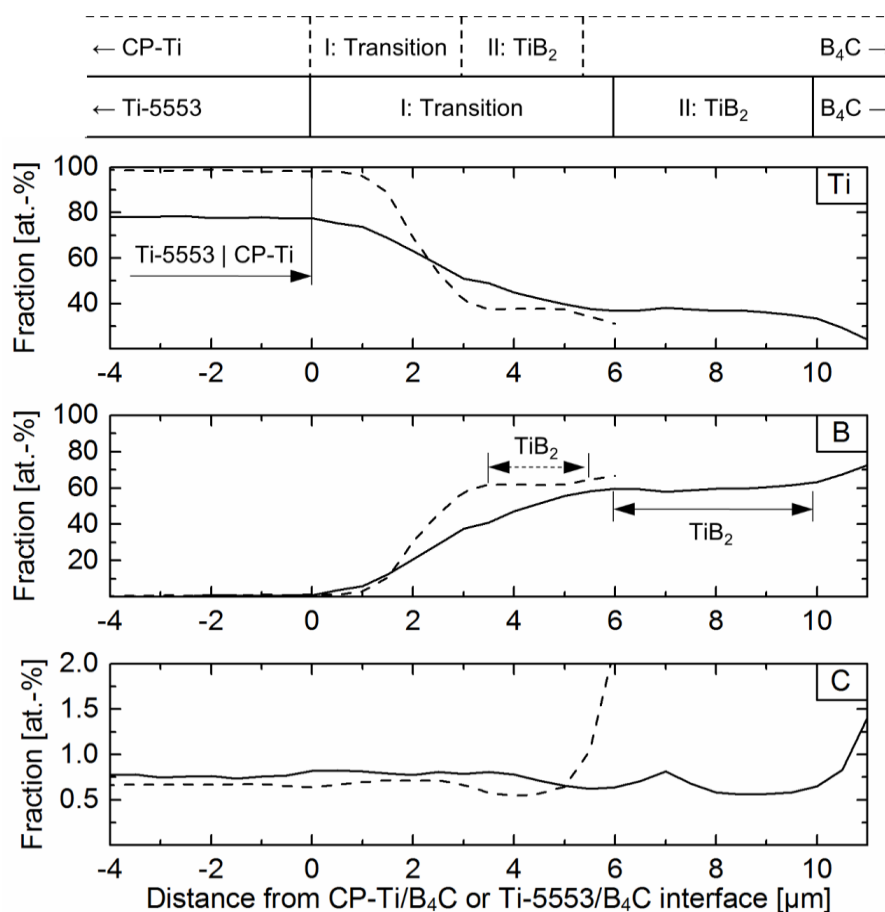


Figure 4. Electron probe microanalysis (EPMA) line scans of the CP-Ti/ B_4C (dashed line) and Ti-5553/ B_4C (solid line) interface showing the distributions of Ti, B and C.

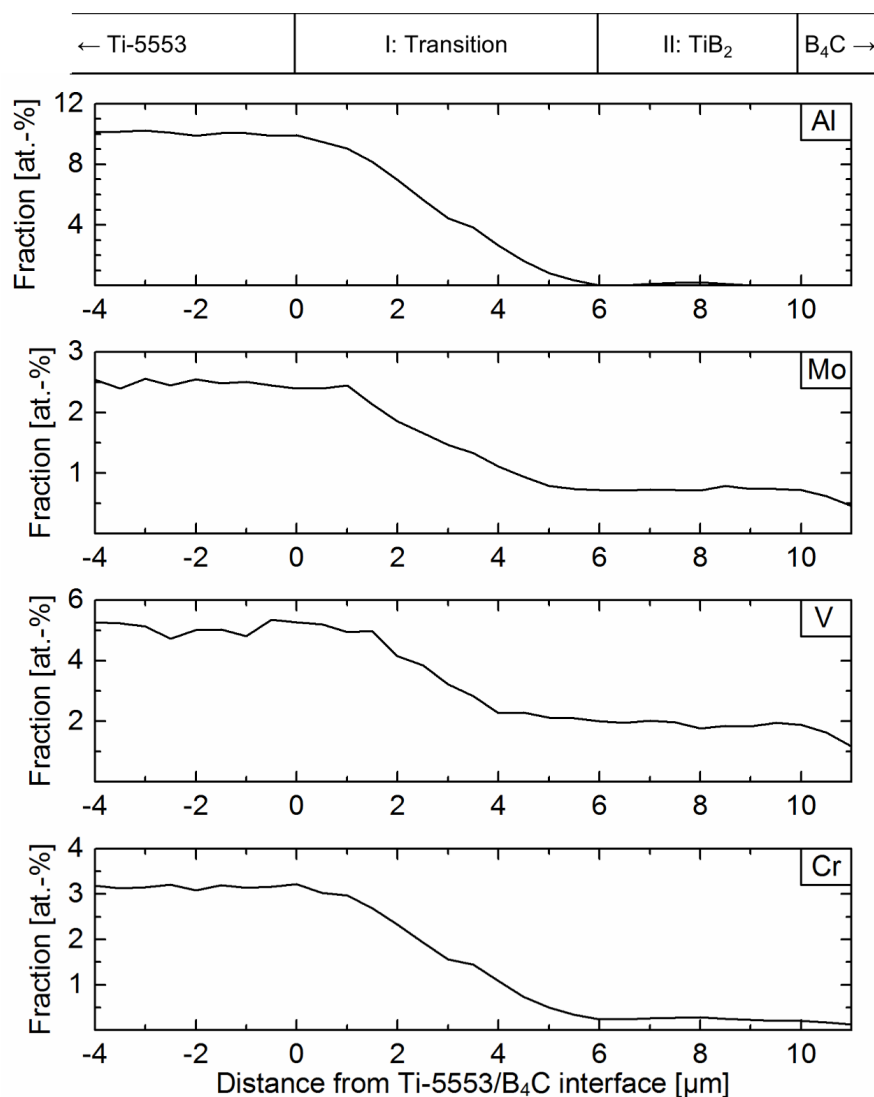


Figure 5. EPMA line scans of the Ti-5553/B₄C interface showing the distributions of Al, Mo, V and Cr.

In summarizing the diffusion experiments, it can be stated that the thickness of the reaction layer between B₄C and Ti-5553 increased compared to that between B₄C and CP-Ti. The alloying elements Mo, V and Cr formed solid solutions within the TiB₂ region in particular and, hence, seemed to effect the retardation of the reaction kinetics around the B₄C conversion. This could be an explanation for the predominant location of the TiB and TiC reinforcing particles close to the initial locations of the B₄C particles at the Ti-5553 particle surfaces.

The results of the XRD phase analysis experiments are shown in Table 5, where the phase fractions were derived from the XRD pattern presented in Figure 6. No traces of residual B₄C and/or graphite were detected by XRD, although these phases were present in the microstructure of the consolidated TMC samples. This was probably due to their phase contents being below the detection limit of XRD analysis in association with the aforementioned particle break-out during sample preparation. With respect to the targeted total ceramic content of 12 vol.-% it should be noted that significantly higher contents were measured within the composites TMC-A and TMC-B, although these TMCs contained unreacted B₄C and/or graphite particles after the consolidation. This was directly associated with the actual stoichiometry of the TiC particles formed. The measured lattice parameters of the TiC within all of the TMC samples exhibited similar values of approx. $4.298 \pm 0.005 \text{ \AA}$, which in turn resulted in a stoichiometry of $y \approx 0.5$ if compared to the data reported in the literature—see

Figure 7. Therefore, the initial powder mixtures of the TMC-B composites did not lead to a balanced molar TiB:TiC ratio, but rather effected a pronounced formation of $TiC_{0.5}$. With respect to the TMC-C composites, the adjustment of the TiB-TiC was almost achieved, although some small amounts of residual graphite, in particular, remained within in the microstructures.

Table 5. Phase compositions of the composites TMC-A, TMC-B and TMC-C determined by X-ray diffraction (XRD).

| Material | Ti-bcc | Ti-hcp | TiB | TiC _y | TiB + TiC |
|-----------------|--------|--------|-----|------------------|-----------|
| | vol.-% | | | | |
| TMC-A (Ti-5553) | 84 | - | 12 | 4 | 16 |
| TMC-A (CP-Ti) | - | 87 | 10 | 3 | 13 |
| TMC-B (Ti-5553) | 86 | - | 7 | 7 | 14 |
| TMC-B (CP-Ti) | - | 85 | 7 | 8 | 15 |
| TMC-C (Ti-5553) | 90 | - | 6 | 4 | 10 |
| TMC-C (CP-Ti) | - | 87 | 8 | 5 | 13 |

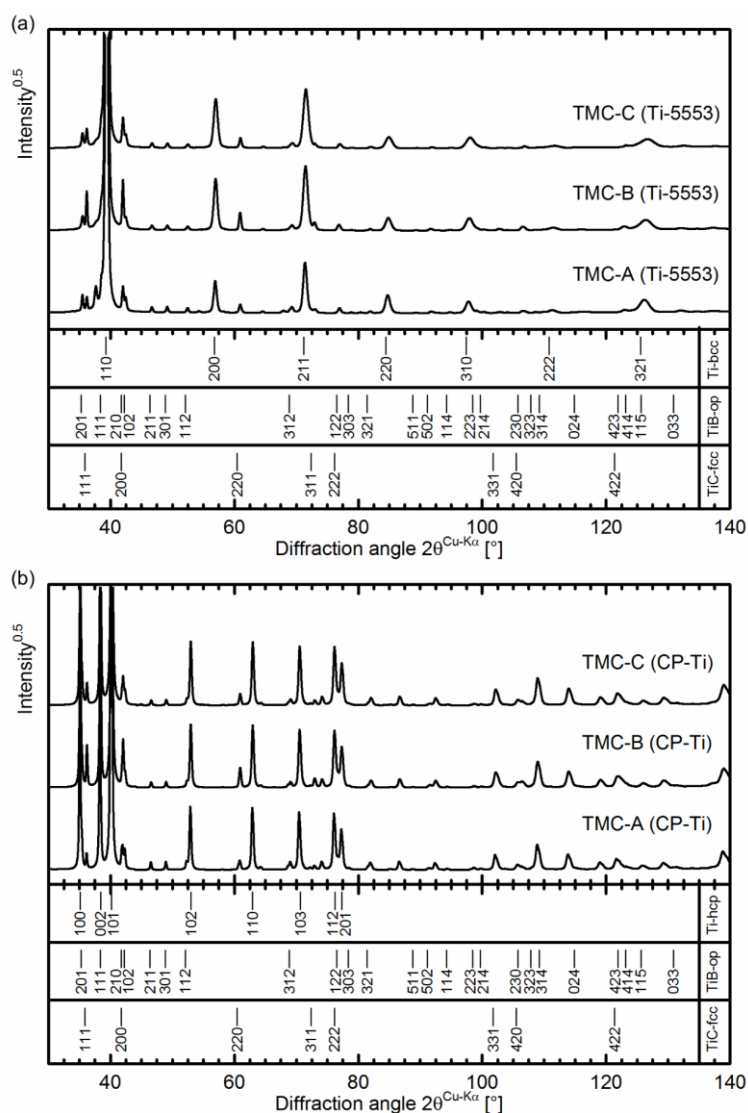


Figure 6. Measured XRD pattern: (a) TMCs based on a Ti-5553 matrix and (b) TMCs based on a CP-Ti matrix.

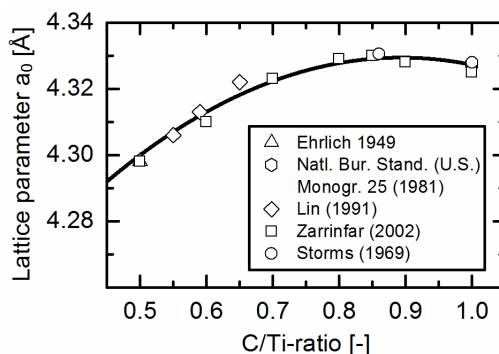


Figure 7. Stoichiometric dependency of the TiC_y lattice parameter a_0 from the molar C/Ti ratio according to literature data [25,41–44].

3.2. Mechanical Properties of the Ti-5553-Based TMCs

Figure 8 shows that the hardness of the TMC-A and TMC-B composites was increased by approximately 20% and for TMC-C by approx. 16% due to the reinforcing particles. Comparing TMC-A and TMC-B, it should be noted that equal values of the hardness were measured despite the latter composite having exhibited a lower total content of particle reinforcements. This can be explained by the different contributions to the macroscopic increase in hardness by the individual phases. With respect to the microhardness of the reinforcements, values reported in the literature are lower for TiB (~1800 HV0.1) than for TiC (~3200 HV0.1) [45]. For the latter, hardness did indeed exhibit a slight correlation with stoichiometry, and declined by roughly 15–20% while decreasing the C/Ti ratio to ~0.5. However, these values are still higher than the TiB values described by Lipatnikov et al. and Sundgren et al. [46,47]. The decrease in measured hardness of the composite TMC-C could be explained by the generally lower total content of particle reinforcement of only 10 vol.-%.

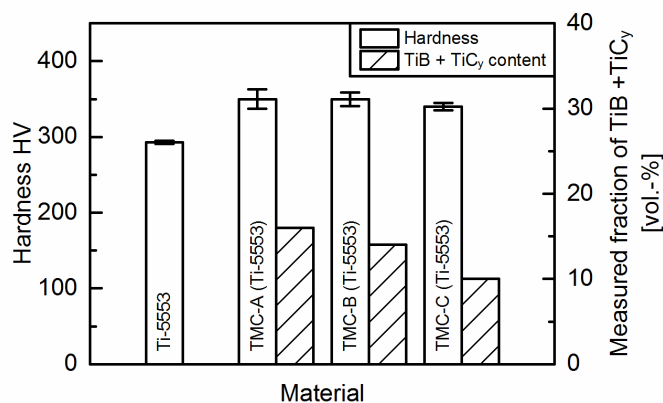


Figure 8. Measured hardness of the TMCs based on Ti-5553 and correlation with the total content of particle reinforcements.

Representative compressive stress-strain curves of the composites in comparison to Ti-5553 are shown in Figure 9. The corresponding values for the compressive yield strength $\sigma_{d0.2}$, the compressive strength σ_{df} and the compressive strain at failure ϵ_{df} are given in Table 6. For all of the TMCs, a strong particle-strengthening effect was observed in comparison to Ti-5553, as the compressive stress level increased by ~23% for TMC-A and ~18% for TMC-B and TMC-C, see Figure 9. However, the $\sigma_{d0.2}$, σ_{df} and ϵ_{df} values of the composites were significantly affected by the total content of the reinforcing particles. Thus, TMC-A (which had the highest total ceramic particle content of 16 vol.-%) exhibited a 5–7% higher compressive yield strength, whereas the ductility was restricted to a value ~30% lower than for TMC-B and TMC-C. Along with the higher ductility, the compressive fracture strength of the

latter composites increased, whereby the composite TMC-C (which had the lowest total content of reinforcing particles) exhibited the highest compressive strength.

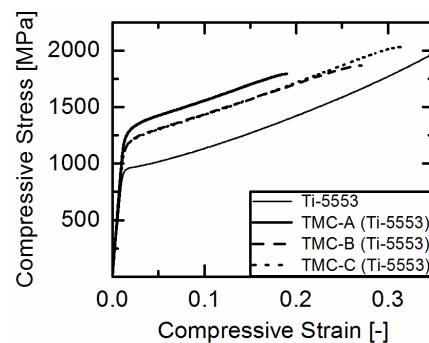


Figure 9. Compressive stress-strain curves of the TMCs and Ti-5553.

Table 6. Measured compressive yield strength $\sigma_{d0.2}$, compressive strength σ_{df} and compressive strain at failure ϵ_{df} of the composites in comparison to Ti-5553.

| Material | $\sigma_{d0.2}$ | σ_{df} | ϵ_{df} |
|-----------------|-----------------|---------------|-----------------|
| | MPa | MPa | % |
| Ti-5553 | 920 ± 20 | 1 | 1 |
| TMC-A (Ti-5553) | 1190 ± 30 | 1780 ± 30 | 17.7 ± 1.1 |
| TMC-B (Ti-5553) | 1110 ± 10 | 1910 ± 60 | 26.7 ± 2.1 |
| TMC-C (Ti-5553) | 1130 ± 10 | 2000 ± 10 | 27.8 ± 2.2 |

¹ no fracture up to a compressive strain of 60%.

Due to the compressive loading, damage became evident in the form of reinforcement particle delamination from the matrix, accompanied by particle fracture of, in particular, the TiB whiskers as a consequence of increasing tensile stresses that occurred during the lateral bulging of the deforming samples, Figure 10a,b. The inability of the ceramic reinforcements to undergo large degrees of plastic deformation (ϵ_{pl}) promoted the initiation of microcracks in the vicinity of the matrix/reinforcement interfaces. As the reinforcement particles were predominantly arranged at the initial Ti-5553 particle interfaces—see Figure 3a,c,e—further crack growth resulted from the subsequent coalescence of these microcracks close to the maximum compressive loading capacity of the composites.

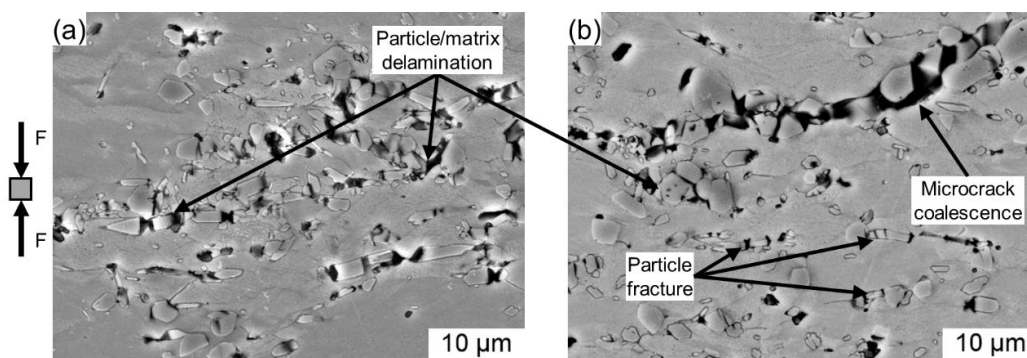


Figure 10. Compression tests of the TMC-B and TMC-C composites interrupted immediately below the maximum loading capacities—damage evolution; (a) TMC-B ($\sigma_{max} = 1900$ MPa, $\epsilon_{pl,max} = 0.25$); (b) TMC-C ($\sigma_{max} = 1960$ MPa, $\epsilon_{pl,max} = 0.26$).

Figure 11a shows representative measured stress-strain responses (σ_b - ε_b) for the composites under 3-point bending conditions, while Table 7 shows the derived bending strengths σ_{bf} , and the outer fiber strains at failure ε_{bf} . Compared to pure Ti-5553, the particle reinforcements within the composite samples effected increases in bending strengths of ~12% (TMC-A) and ~16% (TMC-B and TMC-C), respectively. However, only the composite TMC-A exhibited a considerable decrease in ductility of ~30%, which was indicated by the lower value for ε_{bf} . Interrupted bending tests were carried out immediately below the measured bending strength of the TMCs to identify the mechanisms involved during damage evolution that led to the composites failure. The results were surprising, as no notable instances of microstructural damage were observed in the vicinity of the plane with the maximum bending moment. Only a small number of vertically orientated microcracks within the reaction layers of incompletely reacted B_4C -particle and graphite-particle clusters were found close to the sample surfaces exposed to the maximum tensile stresses during bending, see Figure 11b. These microcracks were strongly oriented perpendicularly to the acting tensile stresses, and were still arrested at the interfaces to the Ti-5553 matrix particles at the moment of test interruption. It was therefore assumed that further increasing the load promoted the growth of these microcracks through the matrix particles within the tensile stress field. Finally, macroscopic cracks suddenly originated from the coalescence of the vertically extending microcracks, resulting in the global fracture of the bending sample. Thus, the bending strength of the composites was primarily related to the tensile strength of the reaction layers surrounding the B_4C -particle and graphite-particle clusters. This could also be an explanation for the minor differences between the bending strengths of the composites, unlike the strengths measured in the compression tests, which showed a dependency on the total reinforcement particle content.

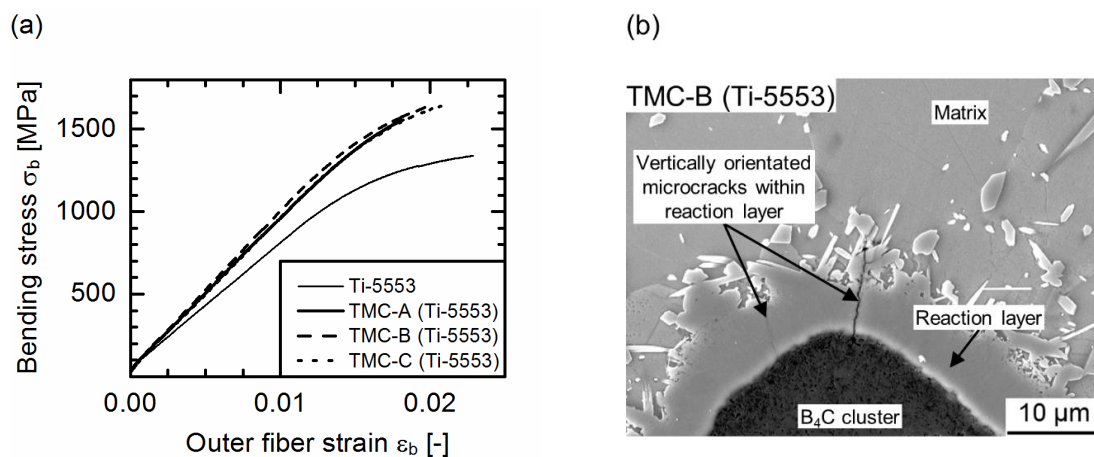


Figure 11. Bending tests: (a) σ_b - ε_b curves under 3-point-bending conditions; (b) crack initiation by tensile failure of the reaction layer attached to an incompletely converted particle cluster.

Table 7. Bending strength σ_{bf} , outer fiber strain at failure ε_{bf} and bending modulus E_b of the composites in comparison to Ti-5553.

| Material | σ_{bf} | ε_{bf} | E_b |
|-----------------|---------------|--------------------|-------------|
| | MPa | % | GPa |
| Ti-5553 | 1360 \pm 30 | 2.4 \pm 0.16 | 86 \pm 8 |
| TMC-A (Ti-5553) | 1540 \pm 20 | 1.8 \pm 0.04 | 100 \pm 4 |
| TMC-B (Ti-5553) | 1630 \pm 40 | 2.45 \pm 0.45 | 99 \pm 7 |
| TMC-C (Ti-5553) | 1620 \pm 40 | 2.12 \pm 0.04 | 96 \pm 3 |

The stiffness of the Ti-5553 matrix was improved successfully with a 10–15% increase in E_b through the reinforcing particles within the composites, see Table 7. However, discussing the influences of the

total reinforcement particle content or the molar TiB:TiC ratio is difficult as the standard deviations involved (in the range of 4–10%) are not negligible.

4. Conclusions

The coarse graphite particles did not completely undergo chemical reaction during the solid-state reaction upon SPS. However, a thin TiC_y reaction layer was formed between these graphite particles and the adjacent CP-Ti or Ti-5553 particles. This TiC_y reaction layer is described in the literature as exhibiting decreasing C/Ti ratios according to the equilibrium compositions at the C/TiC interface and the TiC/Ti interface derived from the Ti-C phase diagram. The growth of this reaction layer is sluggish as the diffusivities of both C and Ti in titanium carbide are coupled while the rate of mass transport and, hence, the growth rate of the TiC layer thickness is determined by the low mobility of the titanium [36]. However, the inter-diffusion coefficient of carbon in titanium carbide also decreases with increasing stoichiometry of the TiC_y [35]. Therefore, the graphite powder used in this study contained some particles that were too coarse, and was not suitable for the exact adjustment of the molar TiB:TiC ratio of the reinforcing particles within the TMCs.

With respect to the adjustment of the TiB:TiC ratio within the TMCs, the stoichiometry of the TiC_y particles formed must be taken into account, since non-stoichiometric $\text{TiC}_{0.5}$ instead of stoichiometric TiC results from the solid-state reaction of carbon and titanium. This is important, as most of the literature dealing with TiC particle-reinforced TMCs presumes the formation of stoichiometric TiC and, hence, underestimates the real TiC particle contents that form during the solid-state reactions. Especially with respect to the studies of Lu et al. [28] and Wang et al. [29], their results could be reinterpreted as the reported increases in tensile strength probably occur due to the higher actual $\text{TiC}_{0.5}$ particle contents, and were not a result of the adjusted molar TiB:TiC ratio.

The alloying elements Mo, V and Cr seem to slow down the reaction kinetics with respect to the B_4C conversion through the solid-state reactions during the sintering process. Diffusion experiments at the reaction zone between B_4C and Ti-5553 or CP-Ti showed that the reaction layer thickness between B_4C and Ti-5553 was approximately doubled compared to that with CP-Ti, while the alloying elements Mo, V and Cr formed solid solutions within the titanium boride phases. The more sluggish B_4C conversion in the case of a Ti-5553 matrix was assumed to be attributable to the low diffusivity of boron (originating from the B_4C particles) within TiB_2 in combination with the extended TiB_2 layer thickness.

Despite some incompletely reacted B_4C clusters and graphite particles that were present within the composites, the hardness, compressive strength σ_{df} and the bending strength σ_{bf} of the TMCs based on Ti-5553 were increased successfully due to the reinforcing particles. The hardness values measured increased with the total reinforcement particle contents achieved (TiB + $\text{TiC}_{0.5}$). The TMCs consisting of powder mixtures containing B_4C and graphite particles exhibited lower TiB + $\text{TiC}_{0.5}$ contents compared to the TMC based on the powder mixture that only contained B_4C particles. Hence, the compressive yield strength $\sigma_{d0.2}$ of these composites was slightly lower, whereas considerably higher compressive strengths σ_{df} were measured in association with increased ductilities.

The damage evolution mechanisms were dependent on the loading conditions—i.e., either compressive or bending loading. For the former case within the tensile stress field of the samples exposed to compressive loading, particle fracture and particle delamination from the deformed matrix led to the initiation of microcracks, with failure occurring due to the coalescence of these microcracks under increasing loads. In the case of bending, only some vertically orientated microcracks within the reaction layers of incompletely reacted B_4C -particle and graphite-particle clusters were found close to those sample surfaces that were exposed to the maximum tensile stresses during loading. These microcracks were predominantly orientated perpendicularly to the tensile stresses acting on the sample, and were still arrested at the interface to the Ti-5553 matrix particles. For this reason, it was assumed that further increasing the load promoted the growth of these microcracks through the matrix particles within the tensile stress field. Finally, macroscopic cracks originated suddenly

from the coalescence of the vertically extending microcracks, resulting in the global fracture of the bending samples.

Author Contributions: Data curation, S.G.; Formal analysis, S.G., L.K., M.R. and I.S.; Funding acquisition, I.S.; Investigation, S.G. and M.R.; Methodology, S.G.; Writing—original draft, S.G.; Writing review and editing, L.K., M.R. and I.S.

Funding: This research was funded by the Bundeswehr Research Institute for Materials, Fuels and Lubricants (WIWeB). The funding sponsors had no role in the design of the study; in the collection, analyses, or interpretation of data; nor in the writing of the manuscript. The founding sponsors supported the authors' decision to publish the results.

Acknowledgments: The authors would like to thank the Bundeswehr Research Institute for Materials, Fuels and Lubricants (WIWeB) for financially supporting this study. Special thanks are due to Dietrich Heger and Christian Schimpf (Institute of Materials Science, TU Bergakademie Freiberg) for conducting the EPMA and the XRD measurements.

Conflicts of Interest: The authors declare no conflict of interest.

References

1. Yang, Z.F.; Lu, W.J.; Xu, D.; Qin, J.N.; Zhang, D. In situ synthesis of hybrid and multiple-dimensional titanium matrix composites. *J. Alloys Compd.* **2006**, *419*, 76–80. [[CrossRef](#)]
2. Yanbin, L.; Yong, L.; Huiping, T.; Bin, W.; Bin, L. Fabrication and mechanical properties of in situ TiC/Ti metal matrix composites. *J. Alloys Compd.* **2011**, *509*, 3592–3601. [[CrossRef](#)]
3. Gorsse, S.; Miracle, D. Mechanical properties of Ti-6Al-4V/TiB composites with randomly oriented and aligned TiB reinforcements. *Acta Mater.* **2003**, *51*, 2427–2442. [[CrossRef](#)]
4. Huang, L.J.; Geng, L.; Xu, H.Y.; Peng, H.X. In situ TiC particles reinforced Ti6Al4V matrix composite with a network reinforcement architecture. *Mater. Sci. Eng. A* **2011**, *528*, 2859–2862. [[CrossRef](#)]
5. Tjong, S.; Ma, Z.Y. Microstructural and mechanical characteristics of in situ metal matrix composites. *Mater. Sci. Eng. R* **2000**, *29*, 49–113. [[CrossRef](#)]
6. Carman, A.; Zhang, L.C.; Ivasishin, O.M.; Savvakina, D.G.; Matviychuk, M.V.; Pereloma, E.V. Role of alloying elements in microstructure evolution and alloying elements behaviour during sintering of a near- β titanium alloy. *Mater. Sci. Eng. A* **2011**, *528*, 1686–1693. [[CrossRef](#)]
7. Feng, H.; Zhou, Y.; Jia, D.; Meng, Q.; Rao, J. Growth mechanism of in situ TiB whiskers in spark plasma sintered TiB/Ti metal matrix composites. *Cryst. Growth Des.* **2006**, *6*, 1626–1630. [[CrossRef](#)]
8. Ni, D.R.; Geng, L.; Zhang, J.; Zheng, Z.Z. Effect of B₄C particle size on microstructure of in situ titanium matrix composites prepared by reactive processing of Ti-B₄C system. *Scr. Mater.* **2006**, *55*, 429–432. [[CrossRef](#)]
9. Soboyejo, W.O.; Lederich, R.J.; Sastry, S. Mechanical behavior of damage tolerant TiB whisker-reinforced in situ titanium matrix composites. *Acta Metall. Mater.* **1994**, *42*, 2579–2591. [[CrossRef](#)]
10. Ma, Z.Y.; Tjong, S.C.; Gen, L. In-situ Ti-TiB metal-matrix composite prepared by a reactive pressing process. *Scr. Mater.* **2000**, *42*, 367–373. [[CrossRef](#)]
11. Tjong, S.C.; Mai, Y.-W. Processing-structure-property aspects of particulate- and whisker-reinforced titanium matrix composites. *Compos. Sci. Technol.* **2008**, *68*, 583–601. [[CrossRef](#)]
12. Atri, R.; Ravichandran, K.; Jha, S. Elastic properties of in-situ processed Ti-TiB composites measured by impulse excitation of vibration. *Mater. Sci. Eng. A* **1999**, *271*, 150–159. [[CrossRef](#)]
13. Zhang, J.; Ke, W.; Ji, W.; Fan, Z.; Wang, W.; Fu, Z. Microstructure and properties of insitu titanium boride (TiB)/titanium (Ti) composites. *Mater. Sci. Eng. A* **2015**, *648*, 158–163. [[CrossRef](#)]
14. Jimoh, A.; Sigalas, I.; Hermann, M. In situ synthesis of titanium matrix composite (Ti-TiB-TiC) through sintering of TiH₂-B₄C. *Mater. Sci. Appl.* **2012**, *3*, 30–35. [[CrossRef](#)]
15. Alman, D.; Hawk, J. The abrasive wear of sintered titanium matrix-ceramic particle reinforced composites. *Wear* **1999**, *225–229*, 629–639. [[CrossRef](#)]
16. Kim, I.Y.; Choi, B.J.; Kim, Y.J.; Lee, Y.Z. Friction and wear behavior of titanium matrix (TiB + TiC) composites. *Wear* **2011**, *271*, 1962–1965. [[CrossRef](#)]
17. AlMangour, B.; Grzesiak, D.; Yang, J.-M. In situ formation of TiC-particle-reinforced stainless steel matrix nanocomposites during ball milling: Feedstock powder preparation for selective laser melting at various energy densities. *Powder Technol.* **2018**, *326*, 467–478. [[CrossRef](#)]

18. Wu, C.L.; Zhang, S.; Zhang, C.H.; Zhang, J.B.; Liu, Y. Formation mechanism and phase evolution of in situ synthesizing TiC-reinforced 316L stainless steel matrix composites by laser melting deposition. *Mater. Lett.* **2018**, *217*, 304–307. [[CrossRef](#)]
19. Brodtkin, D.; Kalidindi, S.R.; Barsoum, M.W.; Zavaliangos, A. Microstructural evolution during transient plastic phase processing of titanium carbide-titanium boride composites. *J. Am. Ceram. Soc.* **1996**, *79*, 1945–1952. [[CrossRef](#)]
20. Mogilevsky, P.; Gutmanas, E.Y.; Gotman, I.; Telle, R. Reactive formation of coatings at boron carbide interface with Ti and Cr powders. *J. Eur. Ceram. Soc.* **1995**, *15*, 527–535. [[CrossRef](#)]
21. Zhao, H.; Cheng, Y.-B. Formation of TiB₂-TiC composites by reactive sintering. *Ceram. Int.* **1999**, *25*, 353–358. [[CrossRef](#)]
22. Vallauri, D.; Atías Adrián, I.C.; Chrysanthou, A. TiC-TiB₂ composites: A review of phase relationships, processing and properties. *J. Eur. Ceram. Soc.* **2008**, *28*, 1697–1713. [[CrossRef](#)]
23. Quinn, C.J.; Kohlstedt, D.L. Solid-state reaction between titanium carbide and titanium metal. *J. Am. Ceram. Soc.* **1984**, *67*, 305–310. [[CrossRef](#)]
24. Choi, Y.; Rhee, S.-W. Equilibrium in the reaction of Ti and C to form substoichiometric TiC_x. *J. Mater. Sci. Lett.* **1994**, *13*, 323–325. [[CrossRef](#)]
25. Storms, E.K. (Ed.) *Refractory Materilas: The Refractory Carbides*; Academic Press: New York, NY, USA, 1967; Volume 2.
26. Okamoto, H. C-Ti (Carbon-Titanium). *J. Phase Equilib. Diffus.* **1998**, *19*, 89. [[CrossRef](#)]
27. AlMangour, B.; Grzesiak, D.; Yang, J.-M. In-situ formation of novel TiC-particle-reinforced 316L stainless steel bulk-form composites by selective laser melting. *J. Alloys Compd.* **2017**, *706*, 409–418. [[CrossRef](#)]
28. Lu, W.J.; Zhang, D.; Zhang, X.N.; Wu, R.J.; Sakata, T.; Mori, H. Microstructure and tensile properties of in situ (TiB + TiC)/Ti6242 (TiB:TiC = 1:1) composites prepared by common casting technique. *Mater. Sci. Eng. A* **2001**, *311*, 142–150. [[CrossRef](#)]
29. Wang, M.-M.; Lu, W.-J.; Qin, J.; Ma, F.; Lu, J.; Zhang, D. Effect of volume fraction of reinforcement on room temperature tensile property of in situ (TiB + TiC)/Ti matrix composites. *Mater. Des.* **2006**, *27*, 494–498. [[CrossRef](#)]
30. Grütznert, S.; Krüger, L.; Schimpf, C.; Radajewski, M.; Schneider, I. Microstructure and mechanical properties of in-situ TiB/TiC particle-reinforced Ti-5Al-5Mo-5V-3Cr composites synthesized by spark plasma sintering. *Metall. Mater. Trans. A* **2018**. under review.
31. Young, R. *The Rietveld Method*; Monographs on Crystallography 5; Oxford University Press: Oxford, UK, 2002; p. 298. ISBN 9780198559122.
32. Lutterotti, L.; Matthies, S.; Wenk, H.R. MAUD: A friendly Java program for material analysis using diffraction. *Newslett. CPD* **1999**, *21*, 14–15.
33. Hayun, S.; Kalabukhov, S.; Ezersky, V.; Dariel, M.P.; Frage, N. Microstructural characterization of spark plasma sintered boron carbide ceramics. *Ceram. Int.* **2010**, *36*, 451–457. [[CrossRef](#)]
34. Vansant, C.A.; Phelps, W.C. Carbide formation from beta-titanium and graphite. *Trans. ASM Q* **1966**, *59*, 105–112.
35. Loo, F.J.J.; Bastin, G.F. On the diffusion of carbon in titanium carbide. *Metall. Trans. A* **1989**, *20*, 403–411. [[CrossRef](#)]
36. Dariel, M.P. Enhanced Mass Transport in Titanium Carbide at Large Departures from Stoichiometry. *Powder Metall. Met. Ceram.* **2003**, *42*, 460–467. [[CrossRef](#)]
37. Wittmann, A.; Nowotny, H.; Boller, H. Ein Beitrag zum Dreistoff Titan-Molybdän-Bor. *Monatsh. Chem. Verwandte Teile And. Wiss.* **1960**, *91*, 608–615. [[CrossRef](#)]
38. Enomoto, M. The B-Ti-V system. *J. Phase Equilib.* **1992**, *13*, 641–644. [[CrossRef](#)]
39. Zdaniewski, W.A. Solid solubility effect on properties of titanium diboride. *J. Am. Ceram. Soc.* **1987**, *70*, 793–797. [[CrossRef](#)]
40. Schmidt, H.; Borchardt, G.; Schmalzried, C.; Telle, R.; Weber, S.; Scherrer, H. Self-diffusion of boron in TiB₂. *J. Appl. Phys.* **2003**, *93*, 907–911. [[CrossRef](#)]
41. Ehrlich, P. Über die binären Systeme des Titans mit den Elementen Stickstoff, Kohlenstoff, Bor und Beryllium. *Z. Anorg. Chem.* **1949**, *259*, 1–41. [[CrossRef](#)]
42. Hubbard, C.R. *Standard X-ray Diffraction Powder Patterns: Section 18—Data for 58 Substances*; Monogram 25—Section 18; National Bureau of Standards: Washington, DC, USA, 1981; Volume 18.

43. Lin, Y.; Zee, R.H.; Chin, B.A. In situ formation of three-dimensional TiC reinforcements in Ti-TiC composites. *Metall. Mater. Trans. A* **1991**, *22*, 859–865. [[CrossRef](#)]
44. Zarrinfar, N.; Shipway, P.H.; Kennedy, A.R.; Saidi, A. Carbide stoichiometry in TiC_x and Cu-TiC_x produced by self-propagating high-temperature synthesis. *Scr. Mater.* **2002**, *46*, 121–126. [[CrossRef](#)]
45. Chandran, K.S.R.; Panda, K.B.; Sahay, S.S. TiBw-Reinforced Ti Composites: Processing, Properties, Application Prospects, and Research Needs. *JOM J. Miner. Met. Mater. Soc.* **2004**, *56*, 42–48. [[CrossRef](#)]
46. Lipatnikov, V.N.; Rempel, A.A.; Gusev, A.I. Atomic ordering and hardness of nonstoichiometric titanium carbide. *Wear Resist. Mater. S. Afr. Ind.* **1997**, *15*, 61–64. [[CrossRef](#)]
47. Sundgren, J.-E.; Johansson, B.-O.; Karlsson, S.-E.; Hentzell, H. Mechanisms of reactive sputtering of titanium nitride and titanium carbide II: Morphology and structure. *Thin Solid Films* **1983**, *105*, 367–384. [[CrossRef](#)]



© 2018 by the authors. Licensee MDPI, Basel, Switzerland. This article is an open access article distributed under the terms and conditions of the Creative Commons Attribution (CC BY) license (<http://creativecommons.org/licenses/by/4.0/>).